Petroleum Science 23 (2026) 3932–3946

Contents lists available at ScienceDirect

Petroleum Science

journal homepage: www.keaipublishing.com/en/journals/petroleum-science

Original Paper

Progressive pseudo-label self-supervised waveform inversion and imaging based on multiscale strategies: A marine data case application

Wen-Da Li [a], Hao Zhang [b,*], Shou-Dong Huo [a,c], Jian-Guang Han [d]

[a] Key Laboratory of Deep Petroleum Intelligent Exploration and Development, Institute of Geology and Geophysics, Chinese Academy of Sciences, Beijing, 100029, China
[b] Institute of Geomechanics, Chinese Academy of Geological Sciences, Beijing, 100081, China
[c] University of Chinese Academy of Science, Beijing, 100049, China
[d] Chinese Academy of Geological Sciences, Beijing, 100037, China

ARTICLE INFO

Article history:
Received 12 August 2025
Received in revised form
6 February 2026
Accepted 6 March 2026
Available online 11 March 2026

Edited by Meng-Jiao Zhou

Keywords:
Machine learning
Full waveform inversion
Migration imaging

ABSTRACT

Full waveform inversion (FWI) and reverse time migration (RTM) have shown great potential in subsurface imaging, yet they remain challenged by migration artifacts and limited deep illumination. A novel PPS-DLI (progressive pseudo-label self-supervised deep learning inversion) framework is proposed that integrates deep learning with multi-scale waveform inversion and imaging. The approach introduces a progressive model-based pseudo-label self-supervised strategy that iteratively refines velocity models by leveraging predictions from previous network stages. Combined with a frequency-based multi-scale inversion scheme, the method enables robust background velocity reconstruction at low frequencies and detailed imaging at higher frequencies. Numerical experiments demonstrate that PPS-DLI significantly reduces the migration artifacts, provides additional structural information with better illumination, improves the deep layers and sub-salt imaging, and preserves amplitude fidelity for enhanced lithological interpretation. These advantages position PPS-DLI as a powerful tool for high-resolution and noise-resistant seismic imaging.

1. Introduction

Full-waveform inversion (FWI), first introduced by Lailly (1983) and Tarantola (1984), which leverages both the full waveform and amplitude information of the wavefield, has long been regarded as the ultimate holy grail in geophysical inversion imaging (Virieux and Operto, 2009). Over the years, significant advancements have been made in optimization algorithms, multi-scale strategies (Bunks et al., 1995; Fu et al., 2018; Choi and Alkhalifah, 2011; Qu et al., 2018; Guo et al., 2019; Nie et al., 2025), objective function (Chi et al., 2014; Alkhalifah and Choi, 2014; Ha and Shin, 2021; Fang et al., 2024; Wang et al., 2024a), initial model construction, and computational efficiency (Wang et al., 2011; Fang et al., 2020; Berti et al., 2024). Nevertheless, challenges persist, particularly in updating the background velocity in deeper layers. This difficulty arises because, in shallow layers, the energy from direct and diving waves is dominant, driving the velocity update in these regions. In contrast, in deeper layers, the energy responsible for updating the background velocity is considerably weaker, with the update being more influenced by reflections at the interfaces. As a result, the background velocity update in deeper layers remains limited. Furthermore, FWI's reliance on waveform fitting makes it highly sensitive to poor data quality and inaccurate initial models, rendering it prone to non-convergence in such scenarios.

Seismic imaging (acquiring subsurface reflectivity models) relies heavily on migration. Migration imaging has been a core technique in seismic data processing since Claerbout (1971), the imaging principle of migration. Migration imaging techniques require good velocity modeling, especially the reverse time migration (RTM) technique, which has the highest requirement for the initial velocity model. In addition, the influence of an inaccurate velocity model, offset aperture, and inverse pseudo-frequency

* Corresponding author.
E-mail address: zhhao@cags.ac.cn (H. Zhang).
Peer review under the responsibility of China University of Petroleum (Beijing).

https://doi.org/10.1016/j.petsci.2026.03.011
1995-8226/

parameter will generate migration artifacts, which affect the reduction accuracy of subsurface reflectivity.

FWI-imaging (Huang et al., 2021; McLeman et al., 2023) is a novel approach that integrates full-waveform inversion (FWI) with migration, by extending FWI to high-frequency bands closely to imaging, and extracting reflection coefficients from the final inversion results. Although FWI-imaging is still in its early stages of development, its potential remains promising, requiring further advancements for more impactful results.

In this paper, we propose leveraging deep learning-based inversion techniques in conjunction with FWI-imaging, aiming to address the challenges traditionally associated with both FWI and migration. The rapid progress of deep learning techniques has led to numerous studies integrating convolutional neural networks (CNNs) with seismic waveform inversion. The first approach mainly focuses on using CNNs to reveal the hidden connection between seismic data and velocity models, such as mapping observed data or migration images to accurate velocity models (e.g. Wu et al., 2018; Yang and Ma, 2019; Wang and Ma, 2020; Liu et al., 2021; Taufik et al., 2024; Wang et al., 2023; Zhang and Gao, 2021; Zhang et al., 2021; Wu et al., 2021, 2022; Wang et al., 2024b). The second approach leverages deep learning as a complement to traditional inversion methods, including generating low-frequency data (Plotnitskii et al., 2020; Cheng et al., 2024), physics-informed simulations (Waheed et al., 2021; Song and Alkhalifah, 2021; Zhang et al., 2023; Rasht-Behesht et al., 2022; Schuster et al., 2024), and reparameterization techniques (Wu and McMechan, 2019; He and Wang, 2021; Zhu et al., 2022; Jiang et al., 2023; Zhao et al., 2025).

In this study, we build upon the concept of FWI-imaging by integrating deep learning with waveform inversion and imaging, and propose a multi-scale inversion imaging framework grounded in pseudo-label self-supervised learning. This approach comprises two key components: a progressive self-supervised strategy and a multi-scale inversion scheme. The progressive pseudo-label self-supervised strategy involves the iterative construction of a velocity dataset required for network training, initially based on model segmentation of the starting velocity model. As iterations proceed, model segmentation is guided by predictions from the preceding network stage, enabling the generation of increasingly accurate velocity models. In this context, "progressive" refers to model segmentation driven by prior network predictions in each iteration, enabling the construction of increasingly accurate velocity models. The multi-scale inversion strategy employs a frequency-based approach, starting with the inversion of the background velocity at low frequencies and gradually transitioning to the higher-frequency bands required for imaging. Numerical tests demonstrate that our method enhances deep illumination and provides clearer sub-salt imaging. Furthermore, the concept of "FWI-imaging" enables precise extraction of the subsurface reflection model while effectively suppressing migration artifacts.

The PPS-DLI imaging method presented in this paper offers several notable advantages: 1) It significantly reduces migration artifacts compared to RTM and traditional migration techniques. 2) By preserving amplitude characteristics, this approach facilitates lithological interpretation through the energy features of the imaged axes, unlike conventional migration methods. 3) It more effectively captures deeper layers of geological features in comparison to FWI imaging. These benefits position the proposed method as a valuable tool in seismic interpretation.

2. Methodology

The Methods section delineates the paper's methodology in three parts: the first two detail the progressive pseudo-label self-supervised deep learning inversion strategy and the multi-scale inversion approach, while the final part emphasizes the importance of FWI-imaging and its connection to our deep-learning-based inversion imaging.

2.1. The progressive model-based pseudo-label self-supervised strategy

We first present the basic theoretical and technical details of the progressive pseudo-label self-supervised deep learning inversion (PPS-DLI) of this paper. We begin by presenting the foundational theoretical and technical aspects of the progressive pseudo-label self-supervised deep learning inversion (PPS-DLI) method outlined in this paper. PPS-DLI comprises two essential components: self-supervision and progression. A clear grasp of both is key to understanding the core principles of PPS-DLI.

We begin with self-supervision. In current end-to-end deep learning inversion techniques, the primary challenge lies in constructing a comprehensive training set that encompasses all subsurface features to model the complex nonlinear equations from raw data to the velocity model. However, achieving this in practice often remains unrealistic.

In this paper, "self-supervised" is used in a geophysical inversion context, which differs from its conventional definition in computer vision. Here, it refers to the automatic generation of training labels from the initial velocity model (derived from observed seismic data) without external ground-truth or pre-existing labeled datasets. The supervision is "self-derived" through progressive refinement: each iteration uses the method's own predictions to generate improved training samples, forming a fully data-driven, self-contained workflow.

In contrast, our pseudo-label self-supervised approach initiates with an initial velocity model and trains the inversion network by creating a training set with background velocities similar to the initial model but enriched with reflective information through model segmentation. Unlike the idealized large-data scenario, our method effectively reduces prediction complexity.

The second component is progression. Our PPS-DLI follows a continuous, iterative inversion process. Beginning with self-supervision from the initial model, the inversion network generates results from the first iteration, which are then used as the basis for the second iteration's self-supervision. This progressive iteration continues until convergence is achieved. We now describe this iterative process in detail, along with the associated pipeline in Fig. 1.

Fig. 1 outlines the PPS-DLI module's workflow. Orange lines indicate the network's prediction pathway, while blue lines denote the training phase. For an unknown subsurface model, field-collected observation data d_{obs} are acquired. Initial velocity estimates $\widehat{v}_{\mathrm{p},0}$ are obtained through tomography or migration velocity analysis (MVA), producing initial RTM images $I_{x,i}$. The CNN uses a two-channel input, $\{\widehat{v}_{\mathrm{p},0}, I_{x,i}\}_{\mathrm{CNN}}$, integrating the initial velocity model and RTM images for prediction.

The network training process commences. A well-created dataset is pivotal for effective neural network training. We generate a training set comprising perturbed models with consistent background velocity but enhanced reflective features derived from the initial model, following model segmentation as described in (Wu et al., 2022). After segmentation, we obtain 24 training models with P-wave reflections, $V_{\mathrm{p,parcellation}} = [V_{\mathrm{p1}}, V_{\mathrm{p2}} \ldots, V_{\mathrm{p24}}]$, which serve as accurate representations during training. Fig. 2 illustrates examples of the training velocity models at different iterations. The first iteration (Fig. 2(a)) uses models derived from segmentation of the initial velocity model, while

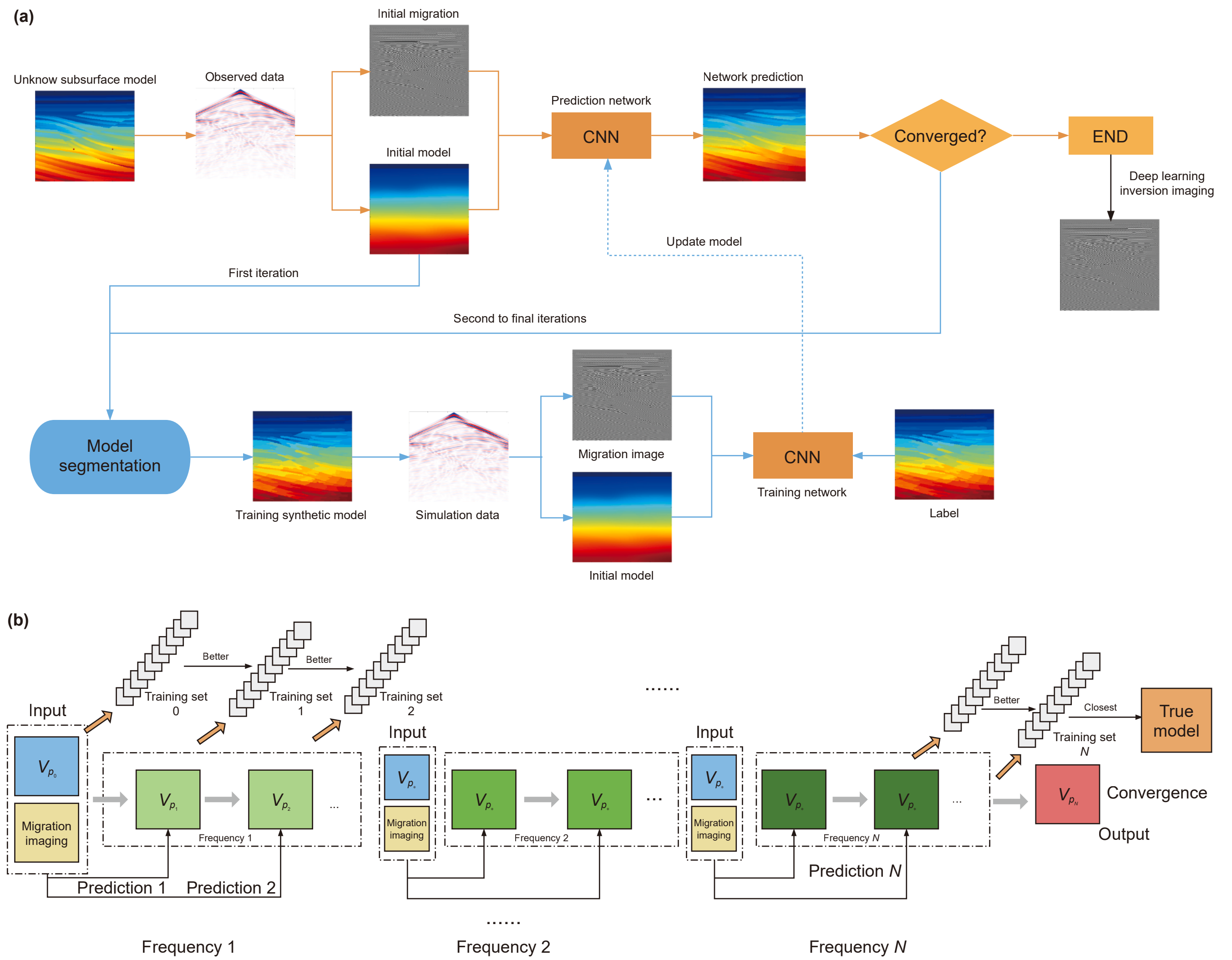

Fig. 1. The workflow of progressive pseudo-label self-supervised deep-learning inversion (PPS-DLI). **(a)** Illustration of the progressive pseudo-label self-supervised strategy within a single frequency band, showing the iterative refinement of training datasets and network predictions. The network predicts velocity models, which are then converted to reflectivity images using Eq. (4) for the final imaging results. **(b)** Complete PPS-DLI framework integrating the multi-scale inversion scheme across progressive frequency bands.

subsequent iterations (Fig. 2(b)) progressively refine the training set based on predictions from the previous network stage. This progressive strategy enables the network to iteratively improve velocity model accuracy. Subsequently, we assemble the input data for network training, comprising $\widehat{V}_{\mathrm{p,input}} = [\widehat{V}_{\mathrm{p1}}, \widehat{V}_{\mathrm{p2}} \ldots, \widehat{V}_{\mathrm{p24}}]$ alongside corresponding migration images $I_{x,\mathrm{input}} = [I_{x,1}, I_{x,2} \ldots, I_{x,24}]$. The training labels are the associated segmented models.

Notably, for the initial velocity models in training data, the ideal approach relies on the tomography model derived from simulated data. However, this method is computationally prohibitive. Consequently, in practical network training, Gaussian smoothing is often used as a substitute for tomography. This substitution, however, introduces a challenge: the training process tends to approximate an inverse smoothing procedure, which can hinder the subsequent processing of field data. To address this, we propose a novel strategy for constructing the initial model. This method first smooths the results from model segmentation, followed by thinning, random perturbation, and interpolation, ultimately generating an initial model that closely resembles the tomography results and is better suited for field data adaptation.

Following network optimization, the CNN models $F_{V_{\mathrm{p}}}^{k,i}$ were derived. Using the pre-prepared input dataset $\{\widehat{v}_{\mathrm{p},0}, I_{x,i}\}_{CNN}$, we performed network prediction:

$$v_{\mathrm{p},k+1,i+1} = F_{V_{\mathrm{p}}}^{k,i}\left(\widehat{v}_{\mathrm{p},i}, I_{x,i}, f_i\right) \tag{1}$$

where $v_{\mathrm{p},k+1,i+1}$ represents the P-wave velocity model, with subscript k denoting the iteration number of PPS-DLI at a given inversion frequency, and subscript i indicating the frequency index in the multi-scale inversion. The network directly predicts the velocity model rather than reflectivity. $\widehat{v}_{\mathrm{p},0}$ denotes the initial P-wave velocity model. f_i denots different frequency in multi-scale processing. We input the prediction results of the network into the judgment module to identify whether it converges, which can determine whether the self-supervised iteration is further recursive or ends.

It is important to clarify the role of forward modeling in our framework. Unlike physics-informed approaches that integrate forward modeling into the training loop via automatic differentiation (e.g., Deepwave, Devito), our method uses forward modeling

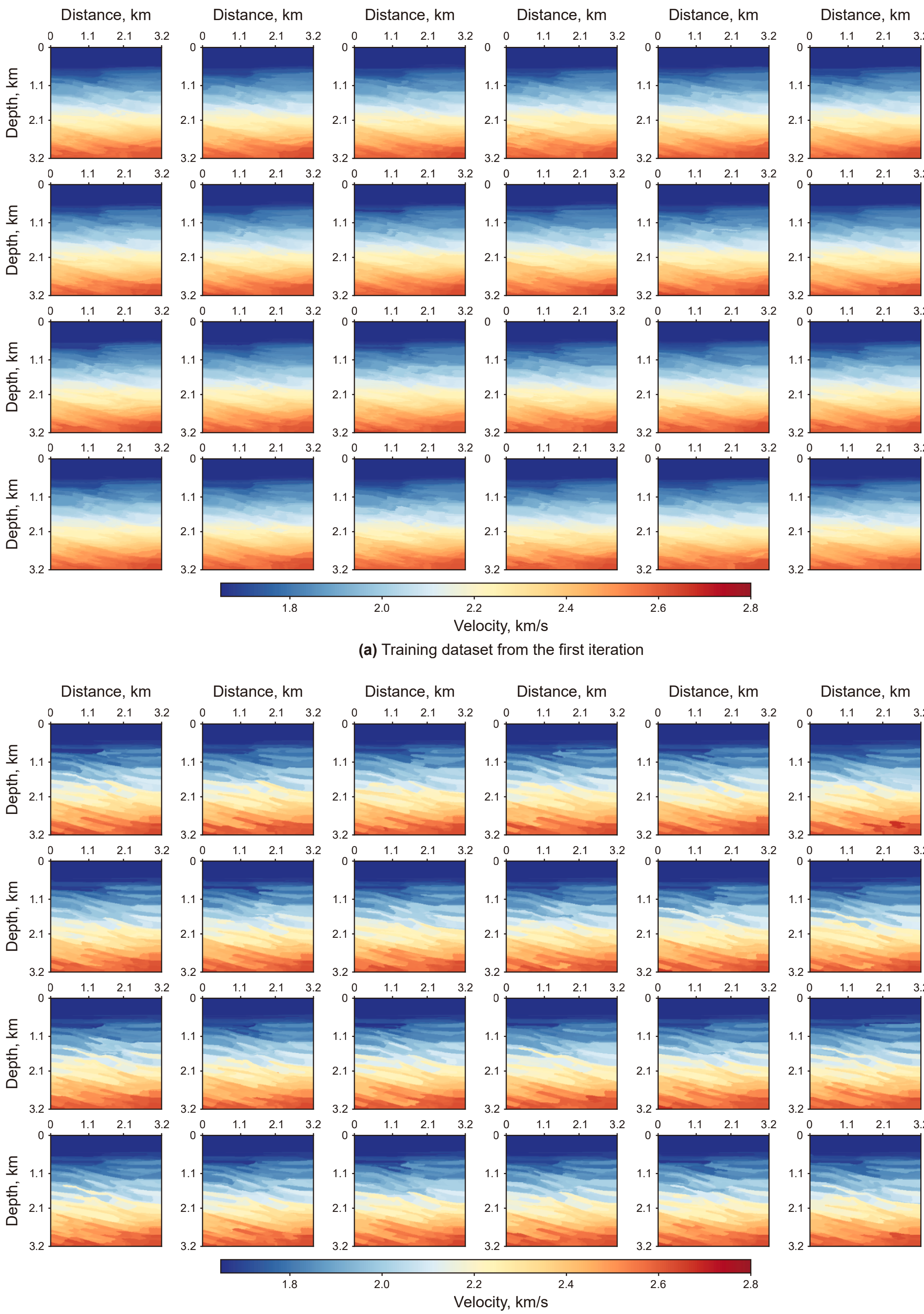

(a) Training dataset from the first iteration

(b) Training dataset from the final iteration

Fig. 2. Examples of training velocity models at different iterations. **(a)** Showing 24 velocity models generated through model segmentation of the initial velocity model. **(b)** Showing 24 velocity models generated based on the prediction results from the previous network stage.

solely for post-iteration convergence assessment. The forward modeling evaluates prediction accuracy by computing data misfit but does not participate in network training or provide gradients to the CNN. The network learns purely from the pseudo-label supervision without physics-based loss constraints.

Before feeding data into the CNN, we apply normalization to ensure training stability. The velocity model uses min-max normalization: $\widehat{v}_{\mathrm{p,norm}} = \left(\widehat{v}_{\mathrm{p}} - \widehat{v}_{\mathrm{p,min}}\right)/\left(\widehat{v}_{\mathrm{p,max}} - \widehat{v}_{\mathrm{p,min}}\right)$, scaling values to [0,1]. The RTM image uses standardization: $I_{x,\mathrm{norm}} = (I_x - \mu_{Ix})/\sigma_{Ix}$, where μ_{Ix} and σ_{Ix} are mean and standard deviation.

2.2. The multi-scale strategy

The multiscale strategy (Fu et al., 2018; Choi and Alkhalifah, 2011; Qu et al., 2018; Guo et al., 2019; Liu et al., 2020) plays a pivotal role in this study. For FWI imaging, inverting directly to the high-frequency bands required for imaging is impractical when the background velocity is constrained. Similarly, in AI inversion, we encounter a comparable challenge. Therefore, adopting a multiscale inversion approach progressing from low to high frequencies emerges as the optimal solution. Firstly, it reduces the uncertainty associated with high-frequency components, which can introduce errors and redundancy in the inversion process. Secondly, it better aligns with physical principles by initially inverting the background velocity with low-frequency data, followed by a gradual reconstruction of fine-scale details using high-frequency information. This is essential for our deep-learning inversion imaging to accurately capture the reflection information in the high-frequency band.

Fig. 3 delineates the workflow.

a. At the start of the inversion, we choose a set of frequencies $f = [f_0, f_1, \ldots, f_i]$ tailored to the seismic data's properties. The inversion follows a multi-step frequency progression, beginning at 6 Hz and incrementally increasing through 15 Hz and 25 Hz during optimization. This approach emphasizes low frequencies initially to define stable velocity constraints before addressing higher-resolution details.
b. For each iteration, a low-pass filter is applied to the observed seismic data, yielding $d_{\mathrm{obs},i} = Lowpass(d_{\mathrm{obs}})$
c. The CNN input is constructed for parameters V_{p}, incorporating reverse time migration (RTM) images I_x (implement the Laplace filtering and depth-dependent illumination compensation after imaging) and initial models $\widehat{v}_{\mathrm{p},0}$. The RTM images are derived from angle-domain RTM imaging.
d. The PPS-DLI framework generates the velocity model for the current iteration.
e. If all frequency steps are completed, the PPS-DLI process concludes. Otherwise, the output data undergoes post-processing using Gaussian smoothing (40–60 iterations with a radius of 3 grid points) to prevent sharp structural anomalies when transitioning between frequency scales, and the smoothed results serve as the base model for the subsequent iteration.

The core inversion equation is as Eq. (1) shows, with the post-processing equation as follows.

$$\widehat{v}_{\mathrm{p},i+1} = Postprocessing\left(v_{\mathrm{p},i+1}\right) \tag{2}$$

where $F^{k,i}_{V_{\mathrm{p}}}$ represent the CNN model, f_i denotes different frequency in multi-scale processing. For multi-scale training, each frequency stage performs up to 5 progressive pseudo-label self-supervised iterations with a constant learning rate (the same optimization

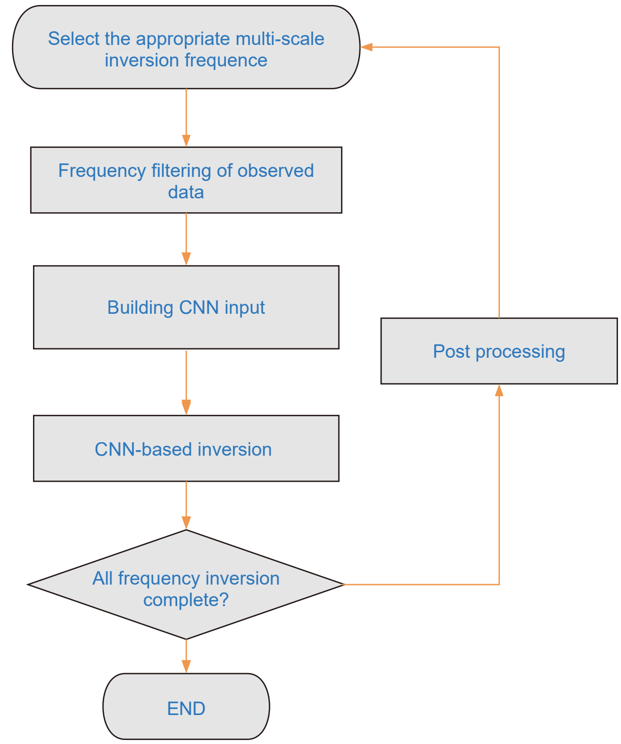

Fig. 3. The workflow of the PPS-DLI method.

method ADAM), as convergence is typically achieved within 3–5 iterations (Fig. 11). Each iteration trains a new network from scratch using the progressively refined training dataset.

Fig. 1(b) illustrates the complete PPS-DLI framework that integrates the progressive pseudo-label self-supervised strategy with the multi-scale inversion scheme. Throughout the entire workflow, the network input remains fixed, consisting of the initial velocity model and RTM images $\{\widehat{v}_{\mathrm{p},0}, I_{x,i}\}$. The key to the progressive refinement lies in the iterative improvement of the training dataset. At each iteration, model segmentation generates training samples based on the prediction from the previous network stage. This process progressively refines the training dataset to approximate the true subsurface model more accurately. As iterations proceed, although the network input stays constant, the evolving training dataset enables the network to learn increasingly accurate velocity-to-structure mappings, ultimately achieving convergence when predictions stabilize.

The multi-scale strategy further enhances this process by progressing from low to high frequencies. At each frequency stage f_i, the progressive self-supervised iterations refine both the background velocity (at low frequencies) and structural details (at higher frequencies). The converged result at frequency f_i serves as the initial model for the next frequency stage f_{i+1} after post-processing, ensuring smooth transitions across frequency bands and enabling the reconstruction of both large-scale velocity structures and fine-scale geological features. Unlike conventional transfer learning approaches that apply pre-trained networks to new data, PPS-DLI trains a new network from scratch for each dataset based on its specific initial velocity model.

2.3. Deep learning inversion imaging

FWI has become one of the most important tools for inverting refined velocity structures, serving a purpose similar to that of

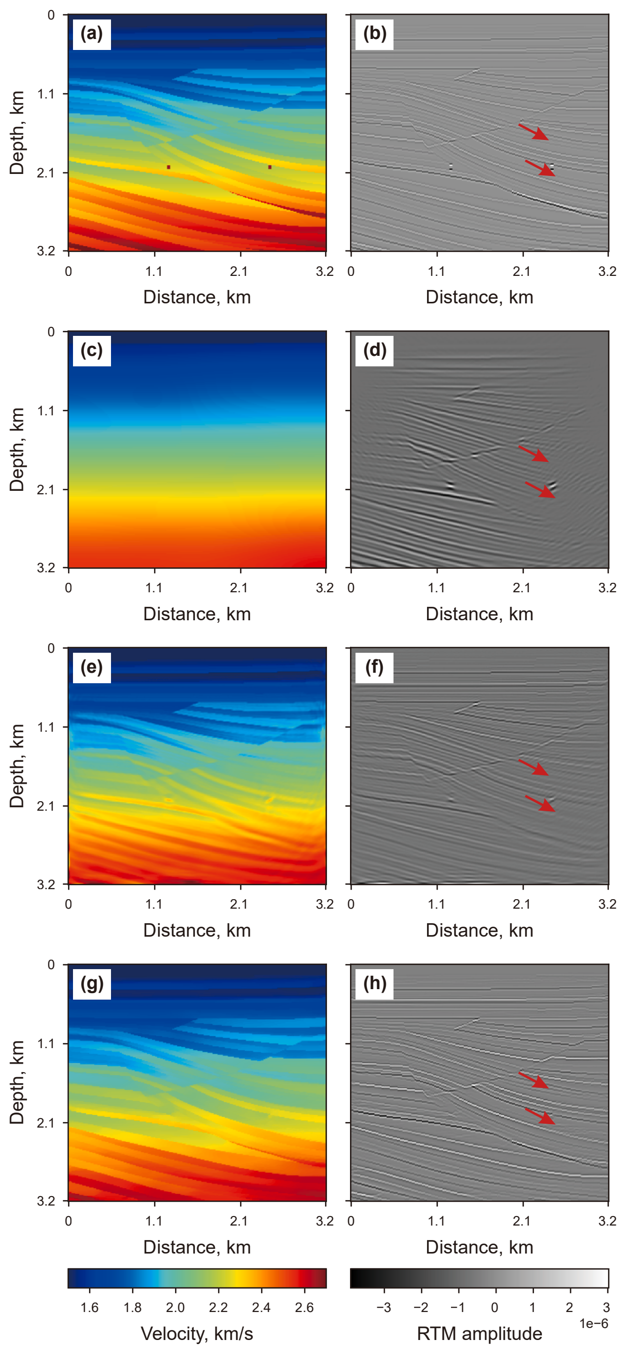

Fig. 4. Comparison of numerical experiments based on PPS-DLI in the Sigsbee model. **(a)** and **(b)** show the real subsurface velocity models along with their corresponding reflection coefficient models. **(c)** and **(d)** display the initial velocity model and its corresponding RTM imaging result. **(e)** and **(f)** present the inversion and imaging results from FWI, respectively. **(g)** and **(h)** illustrate the inversion and imaging results based on PPS-DLI.

reverse-time migration, which is to determine the physical parameters of the subsurface. Depth migration, particularly reverse time migration algorithms, heavily depends on the initial velocity model. Historically, the inversion results have mainly been used as the velocity model for reverse time migration imaging (or other migration algorithms), without establishing a comprehensive process that integrates inversion and imaging.

High-frequency full waveform inversion (FWI) effectively restores structural information of the subsurface medium (Wang et al., 2019), though its influence on waveform simulation and migration imaging remains limited. Nonetheless, velocity modeling that incorporates structural features offers significant insights for tectonic interpretation (Sirgue et al., 2009; Lu, 2016; Shen et al., 2018). Both background velocity characteristics and high-frequency structural data are crucial for geological analysis. One such high-frequency feature, reflectivity, refers to the volume distribution of the reflection coefficient. This coefficient, which is the normalized impedance contrast, can be determined using the following equation:

$$\frac{\partial Z}{\partial n}=\frac{\partial Z}{\partial x}\cos\phi\sin\theta+\frac{\partial Z}{\partial y}\sin\phi\sin\theta+\frac{\partial Z}{\partial z}\cos\theta \tag{3}$$

where Z denotes the impedance, n represents the normal direction to the subsurface reflector. Impedance is defined as the product of density and velocity, $Z=\rho v$, while ϕ and θ represent the azimuth and dip angles of the normal vector to the subsurface reflectors. In this study, we assume density is either constant, concentrating solely on the correlation between reflectivity and velocity (noting that alternative velocity-to-density relationships could also be applied). Consequently, the impedance contrast can be approximated as:

$$\frac{\partial Z}{\partial n}\approx\rho\left(\frac{\partial v}{\partial x}\cos\phi\sin\theta+\frac{\partial v}{\partial y}\sin\phi\sin\theta+\frac{\partial v}{\partial z}\cos\theta\right) \tag{4}$$

The PPS-DLI network outputs a velocity model v_{p} at each iteration. To obtain the reflectivity-based imaging result (PPS-DLI imaging), we apply Eq. (4) to the final predicted velocity model as a post-processing step. Both FWI and PPS-DLI can generate reflectivity models through Eq. (4), which forms the basis of the "FWI-imaging" concept (Huang et al., 2021; Zhang et al., 2020). PPS-DLI imaging, as presented in this study, shares similarities with FWI imaging, both of which produce reflectivity-based images. The benefits of PPS-DLI imaging over traditional migration methods primarily include.

a. Effective suppression of migration imaging noise.
b. High energy fidelity, with distinct energy variations above and below the reflectivity layer, aiding geological interpretations related to lithology and other factors.
c. Reduction of imaging artifacts arising from multiple wave interactions.

It is important to distinguish between the two types of post-processing in our workflow. The post-processing in Eq. (2) refers to velocity smoothing applied during the multi-scale inversion iterations to ensure smooth transitions between frequency stages. In contrast, the post-processing described here (Eq. (4)) is applied only once to the final inverted velocity model to extract the reflectivity-based imaging result.

3. Numerical testing

In the testing section, the study begins with the layer model (Sigsbee) and a basic salt dome model to assess the method's effectiveness, concluding with a real field oceanic data case to evaluate its performance with field data. The synthetic velocity models are scaled at 1:1 to specifically test the method's capability in imaging deep background velocities and reflectivity.

To emphasize the distinctive features of the proposed method, we conduct comparison experiments as follows: first, we compare PPS-DLI with conventional RTM imaging results; second, we compare FWI-imaging from prior studies with the results obtained using the method presented in this paper.

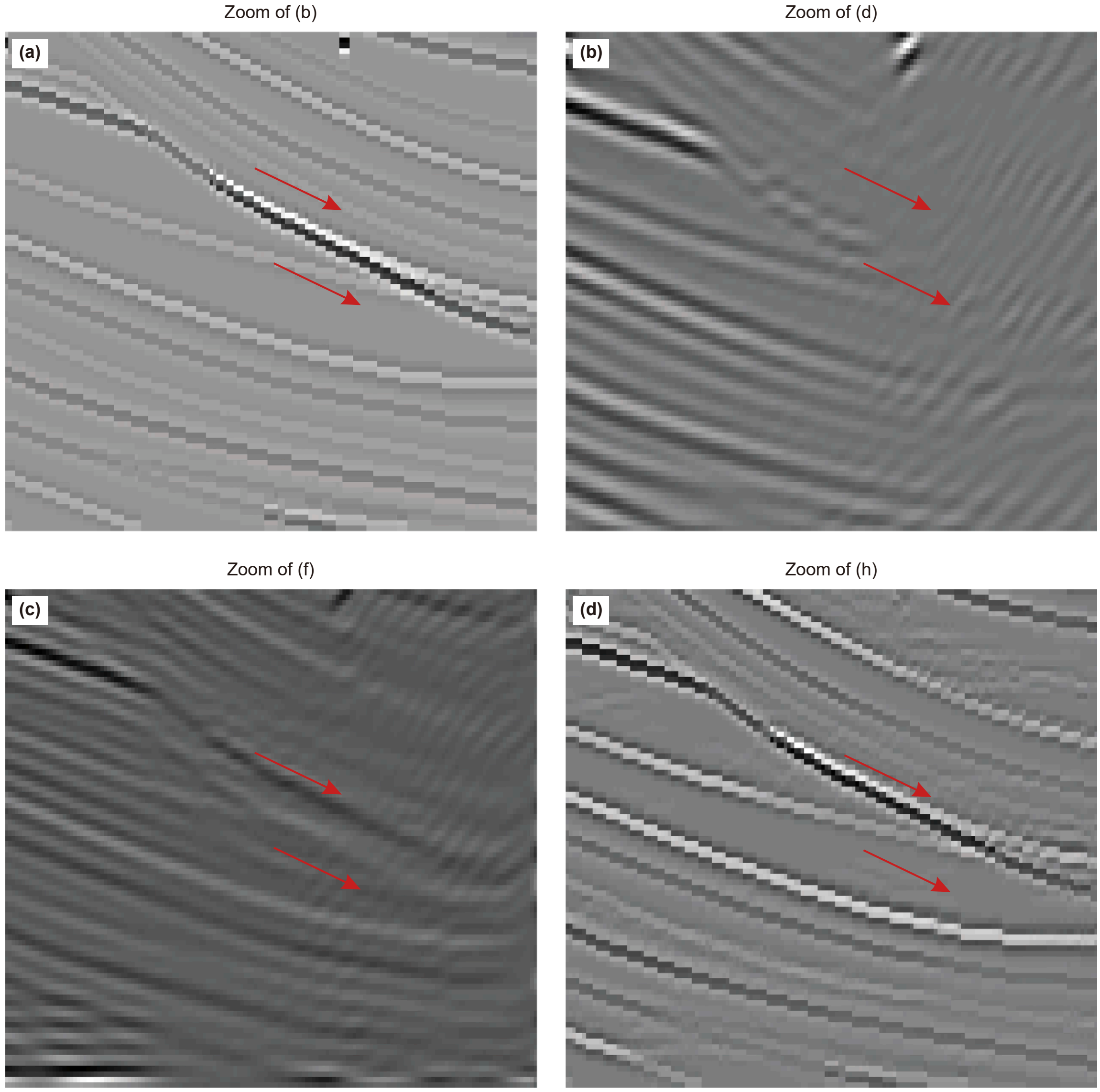

Fig. 5. Localized magnification of the imaging results in (b), (d), (f), and (h) of Fig. 6, respectively.

3.1. Case 1: Sigsbee model numerical testing

First, we compare different imaging methods on the Sigsbee model with the PPS-DLI in this paper. Fig. 4 shows the comparison of numerical experiments based on PPS-DLI in the Sigsbee model. (a) and (b) show the real subsurface velocity models along with their corresponding reflection coefficient models. (c) and (d) display the initial velocity model and its corresponding RTM imaging result. (e) and (f) present the inversion and imaging results from FWI, respectively. (g) and (h) illustrate the inversion and imaging results based on PPS-DLI.

This experimental comparison can be divided into two categories based on its objectives: one focusing on the comparison between conventional RTM imaging and FWI-imaging (AI-imaging) results, and the other on the comparison between FWI-imaging and the AI-imaging (PPS-DLI) method presented in this paper. The paper highlights the proposed method's contribution through two key aspects.

Initially, we compare the inversion outcomes of FWI (Fig. 4(e)) with PPS-DLI (Fig. 4(g)), noting consistent accuracy in the shallow inversion zone (<1.5 km). However, at greater depths, PPS-DLI excels in reproducing background velocity details. FWI's sensitivity to deep velocity information is limited by illumination and sensitive kernel, whereas PPS-DLI adeptly recovers these features through a progressive self-supervision approach and model segmentation strategy. (Given their reliance on multi-scale algorithms, the influence of multi-scale on these methods is not addressed.)

Returning to the imaging results section, we contrast RTM imaging outcomes (Fig. 4(d)) with those of FWI-imaging (Fig. 4(f)) and PPS-DLI-imaging (Fig. 4(h)). The inversion-based imaging effectively reduces migration artifacts generation, as highlighted by the red arrows in Fig. 4. The RTM results obscure the effective axes where migration artifacts is prevalent. Additionally, energy features observed in RTM imaging lack geological significance above and below the isophase axis due to RTM's non-amplitude-preserving nature. Conversely, the PPS-DLI-imaging presented here accurately retains the energy characteristics of the axis, aiding geological lithology interpretation. Notably, FWI-imaging results still show a little residual migration artifacts (although it is

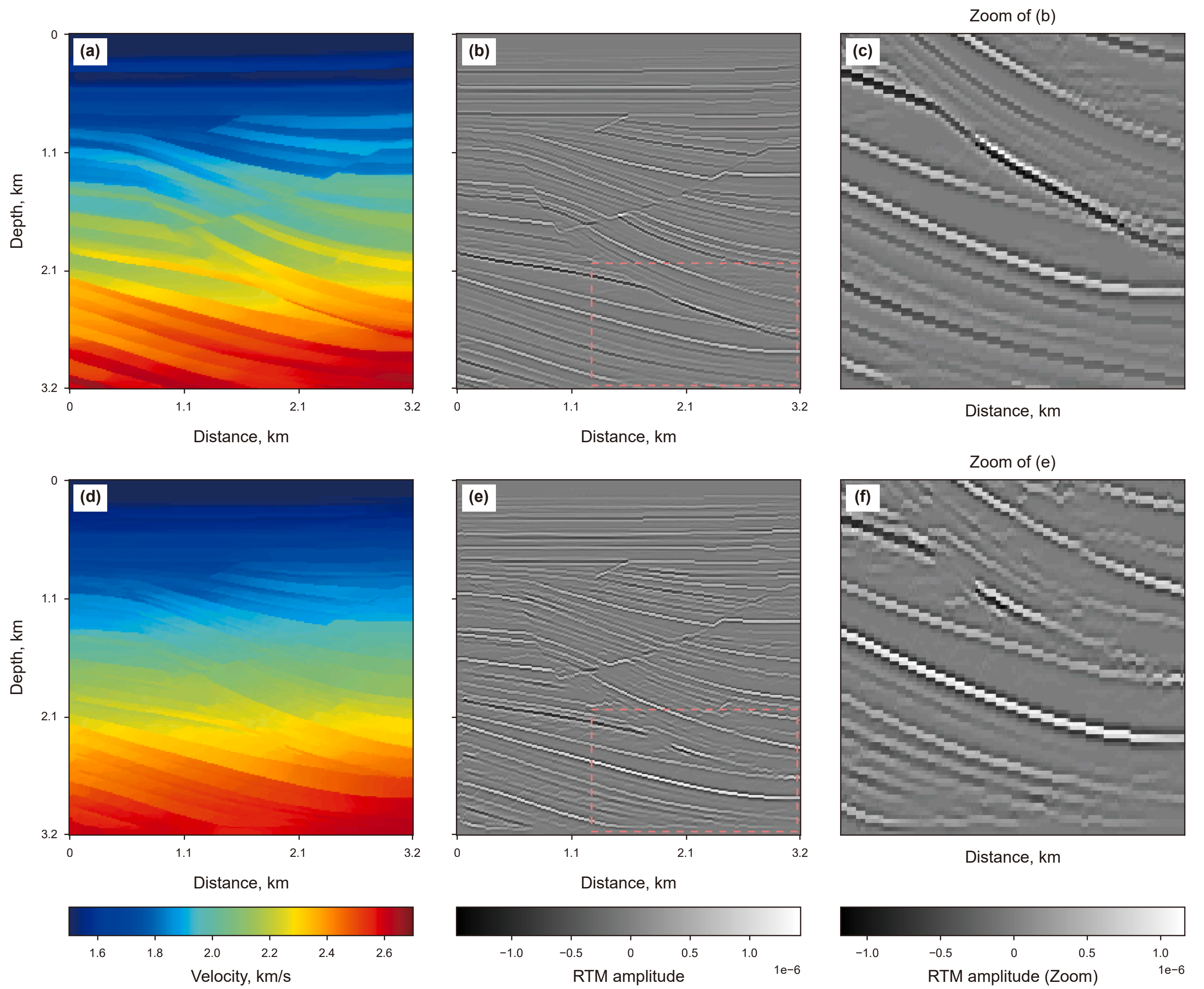

Fig. 6. Comparison between multi-scale and single-frequency inversion strategies on the Sigsbee model. **(a)** Inverted velocity model using multi-scale PPS-DLI. **(b)** PPS-DLI imaging result with multi-scale strategy. **(c)** Localized magnification of (b). **(d)** Inverted velocity model using single-frequency PPS-DLI (25 Hz only). **(e)** PPS-DLI imaging result with single-frequency inversion. **(f)** Localized magnification of (e).

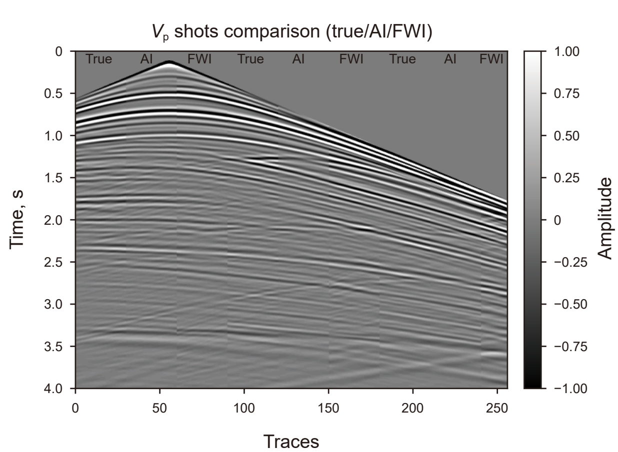

Fig. 7. The forward modeling interleaved display results based on the true, PPS-DLI, and FWI from the Sigsbee model, respectively.

much better than the RTM results), attributed to FWI's use of the adjoint state method, which introduces noise through the correlation of forward and backward wavefield simulations. The PPS-DLI-imaging method, despite utilizing RTM image data during iteration, effectively mitigates this noise through network training and self-supervision.

A comparison of FWI-imaging with PPS-DLI-imaging reveals that the progressive pseudo-label self-supervised approach presented herein more effectively restores deep features, enhancing both imaging clarity and axis continuity. Fig. 5 displays localized magnifications of the results from (b), (d), (f), and (h) in Fig. 4. As indicated by the red arrows, FWI-imaging efficiently mitigates migration artifacts in comparison to RTM, while PPS-DLI-imaging further reduces noise associated with the FWI gradient, providing a more accurate recovery of deep structural features.

To demonstrate the contribution of the multi-scale strategy to progressive self-supervised inversion, we compare multi-scale inversion with single-frequency inversion (direct 0–25 Hz

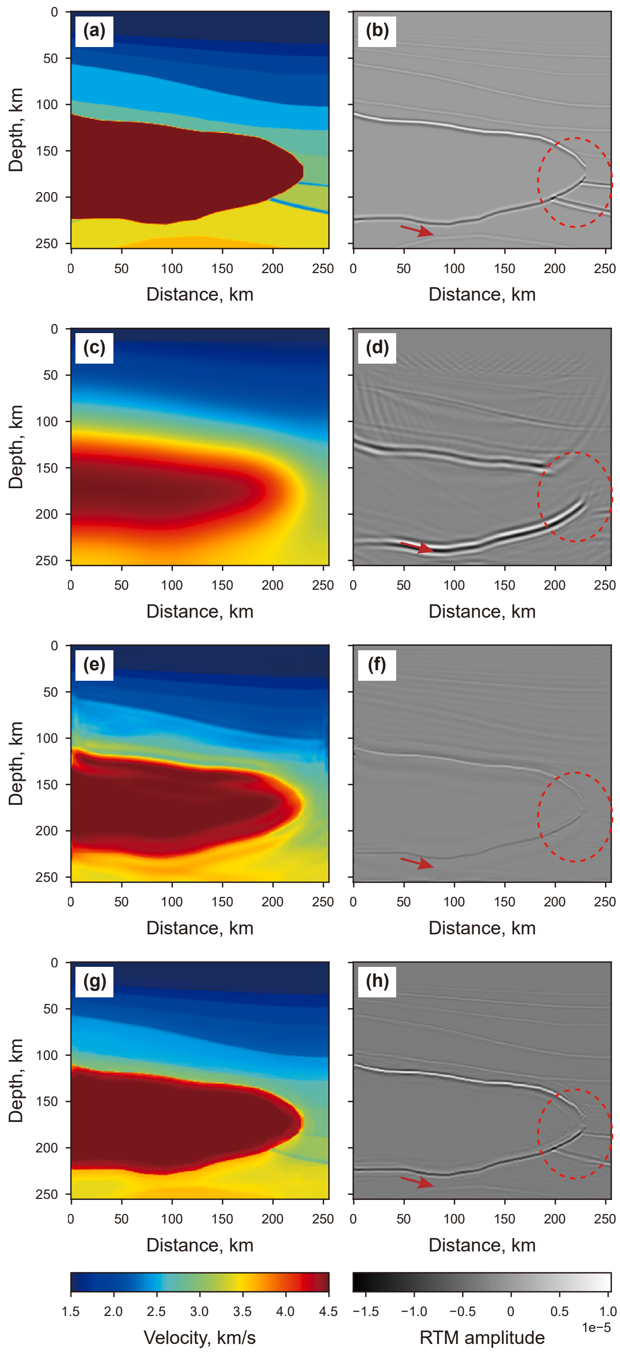

Fig. 8. Comparison of numerical experiments based on PPS-DLI in a basic salt dome model. **(a)** and **(b)** show the real subsurface velocity models along with their corresponding reflection coefficient models. **(c)** and **(d)** display the initial velocity model and its corresponding RTM imaging result. **(e)** and **(f)** present the inversion and imaging results from FWI, respectively. **(g)** and **(h)** illustrate the inversion and imaging results based on PPS-DLI.

inversion without multi-scale progression) on the Sigsbee model (Fig. 6). The multi-scale results (Fig. 6(a)–(c)) show significantly better structural reconstruction than single-frequency inversion (Fig. 6(d)–(f)). The multi-scale approach establishes a robust background velocity at low frequencies before refining structural details at higher frequencies, making it more resilient to initial model inaccuracies. Direct high-frequency inversion struggles when the initial model deviates from the true structure, as it attempts to simultaneously learn both background velocity and fine-scale features. As shown in the zoomed regions (Fig. 6(c) and (f)), the multi-scale strategy yields superior structural continuity and clearer boundaries, particularly at depth. This demonstrates that multi-scale inversion is essential for robust convergence in the PPS-DLI framework.

Fig. 7 shows the forward modeling interleaved display results based on the true, PPS-DLI, and FWI models from the Sigsbee model, respectively. We find that the model forward records obtained through our method show a better overlap with the records of the real model, both in terms of travel time and morphological accuracy. This further demonstrates that the method presented in this paper offers more accurate velocity inversion results compared to traditional FWI.

3.2. Case 2: salt dome model numerical testing

Next, we test the imaging effects of different methods in the salt dome model, focusing mainly on observing how the different methods portray the salt dome boundaries, especially the lower salt dome boundaries, as well as the effects of sub-salt imaging. Fig. 8 shows the comparison of numerical experiments based on PPS-DLI in a basic salt dome model.

A comparison of FWI-imaging with the conventional RTM method reveals that both FWI-imaging and PPS-DLI-imaging effectively mitigate migration artifacts. Furthermore, these methods preserve energy and characterize geological features, such as upper and lower lithology, through energy distribution, a capability not afforded by RTM. These findings align with the conclusions drawn from the previous Sigsbee model comparison.

Next, we examine key aspects of the salt dune model, beginning with the delineation of the salt dune boundary and the imaging effects of sub-salt. As highlighted by the red dashed line in the figure, the method presented herein substantially enhances the definition of the salt dune boundary and the continuity of the deep homophase axis. Moreover, in comparison to the FWI-imaging method (indicated by the red arrows in the figure), the PPS-DLI-imaging technique demonstrates superior capability in reconstructing the subsalt geological structure. Fig. 9 displays localized magnifications of the results from (b), (d), (f), and (h) in Fig. 8. As indicated by the red arrows in the figure, the method presented in this paper not only effectively suppresses migration artifacts and enhances the continuity of the axis, but, more crucially, it also provides a superior reconstruction of the sub-salt structure, offering significant value for hydrocarbon reservoir interpretation, especially when compared to traditional RTM and FWI-imaging techniques. Fig. 10 presents the forward modeling comparison results from the Salt dome experiment, which consistently validate the conclusion demonstrated in Fig. 7.

To better understand the convergence behavior of PPS-DLI, we analyze the error evolution across iterations for both the Sigsbee and salt dome models (Fig. 11). The RMSE curves reveal two important characteristics of the progressive pseudo-label self-supervised strategy.

First, the error consistently decreases with iterations at each frequency stage, demonstrating effective convergence. However, a slight error increase occurs at the first iteration of each new frequency stage (transitions from 6 Hz to 15 Hz and from 15 Hz to 25 Hz). This is attributed to the post-processing (Gaussian smoothing) applied before frequency transitions, which temporarily removes some fine-scale features to ensure smooth velocity transitions between frequency bands. Second, the scatter points showing training dataset errors align with our theoretical analysis – as iterations progress, the training dataset increasingly approximates the true subsurface model. This progressive refinement of the training dataset enables the network to learn more accurate

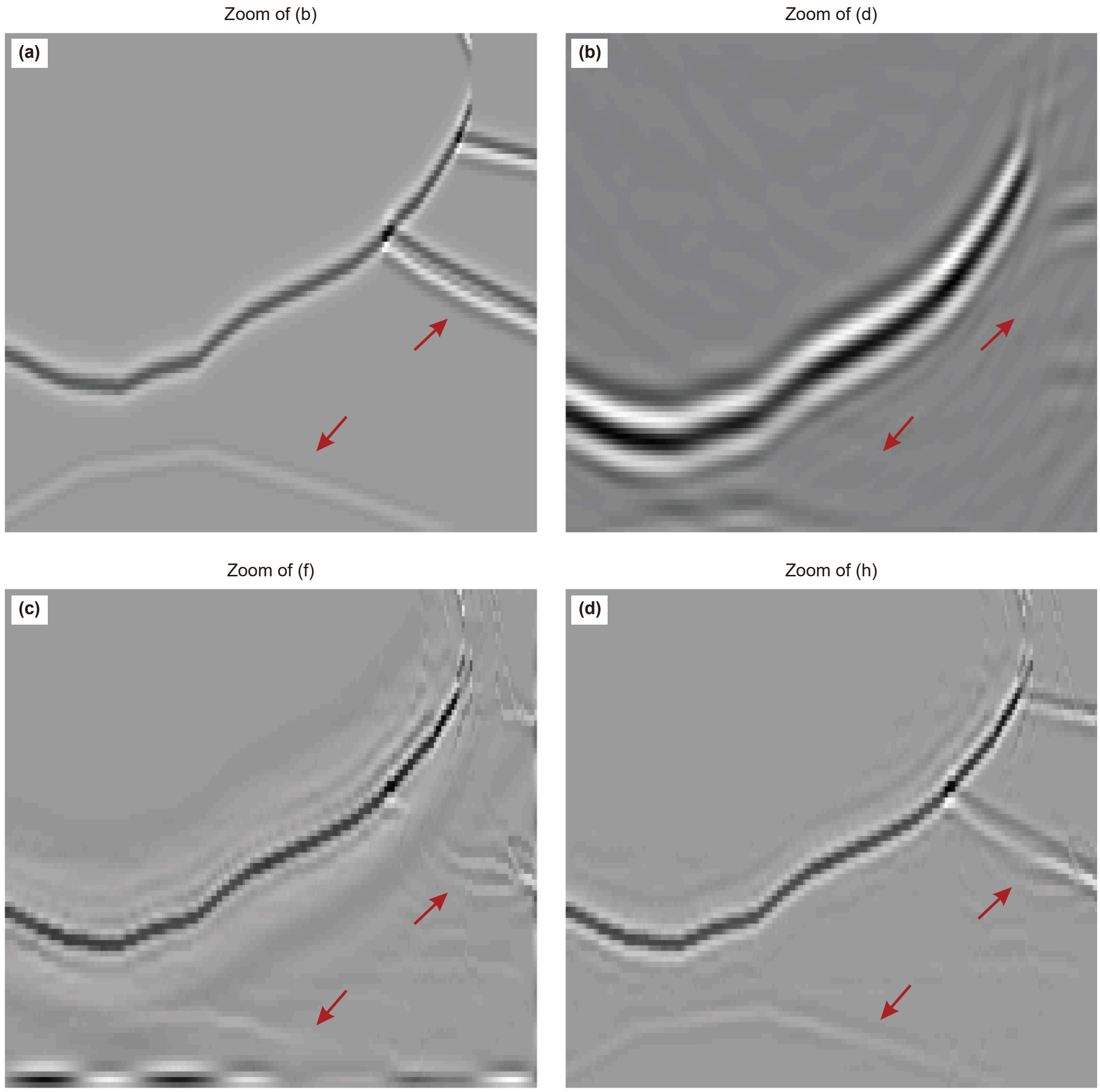

Fig. 9. Localized magnification of the imaging results in (b), (d), (f), and (h) of Fig. 8, respectively.

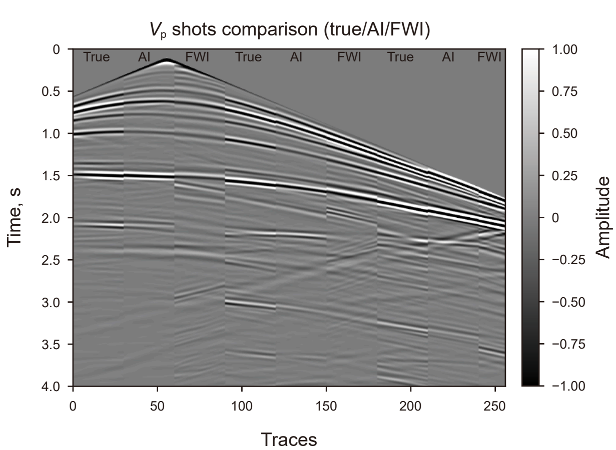

Fig. 10. The forward modeling interleaved display results based on the true, PPS-DLI, and FWI from the salt dome model, respectively.

mappings from initial velocity models to true structures. The training dataset RMSE decreases from approximately 2.5%–2.8% to 1.5%–2.0% for the Sigsbee model and from 7.0% to 4.0%–4.5% for the salt dome model by the final iteration, confirming that the self-supervised strategy successfully generates increasingly realistic training samples.

3.3. Case 3: A marine data case study

Next, we assess the efficacy of the methodology through a multiscale inversion and imaging example based on marine seismic data. Following the same pseudo-label self-supervised training strategy as synthetic examples, we train a new network specifically for this marine dataset. This data is sourced from an offshore field, where the marine subsurface is characterized by predominantly flat layers, interspersed with minor folds and faults. The initial velocity model was derived via tomography velocity inversion (Fig. 12(a)), with values ranging from

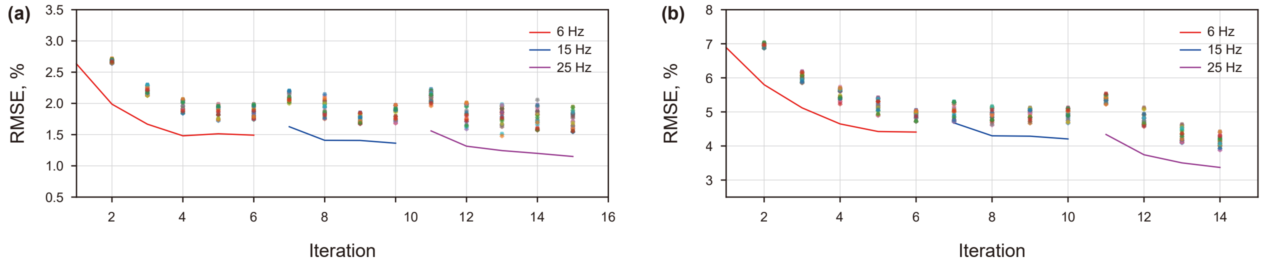

Fig. 11. Convergence analysis of PPS-DLI for the Sigsbee model **(a)** and salt dome model **(b)**. The solid lines represent the RMSE between the predicted velocity model and true model across different frequency stages (6 Hz–red, 15 Hz–blue, 25 Hz–magenta). The RMSE is calculated as: $\mathrm{RMSE}=\frac{\sqrt{\frac{1}{N}\sum_{i=1}^{N}\left[\left(v_{\text{pred}}-v_{\text{true}}\right)^{2}\right]}}{v_{\text{mean}}}\times 100$, where N is the number of grid points, v_{pred} is the predicted velocity, v_{true} is the true velocity, and v_{mean} is the spatial mean of the true velocity model. Scatter points indicate the RMSE between training dataset samples and the true model at each iteration, demonstrating progressive improvement of the training dataset quality.

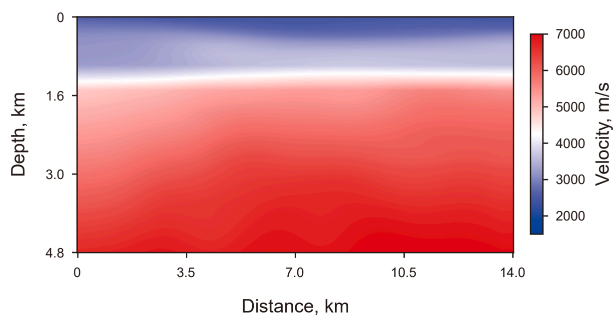

Fig. 12. Initial velocity model of marine field seismic data from tomography inversion.

approximately 1500 to 7000 m/s. The source wavelet was estimated directly from the field data using data-driven approaches. Utilizing this tomography velocity model, we compare the outcomes of FWI and FWI-imaging with those presented in this paper, thereby validating the proposed approach for suppressing migration artifacts and enhancing velocity and structural updates in deeper, poorly illuminated regions through FWI.

By comparing the multiscale FWI inversion results (Fig. 13(a)) with the multiscale PPS-DLI inversion results (Fig. 13(c)), we find that for shallow (<2 km) background velocity and geologic structure information, both methods give good results. Compared to tomography, both methods improve the background velocity

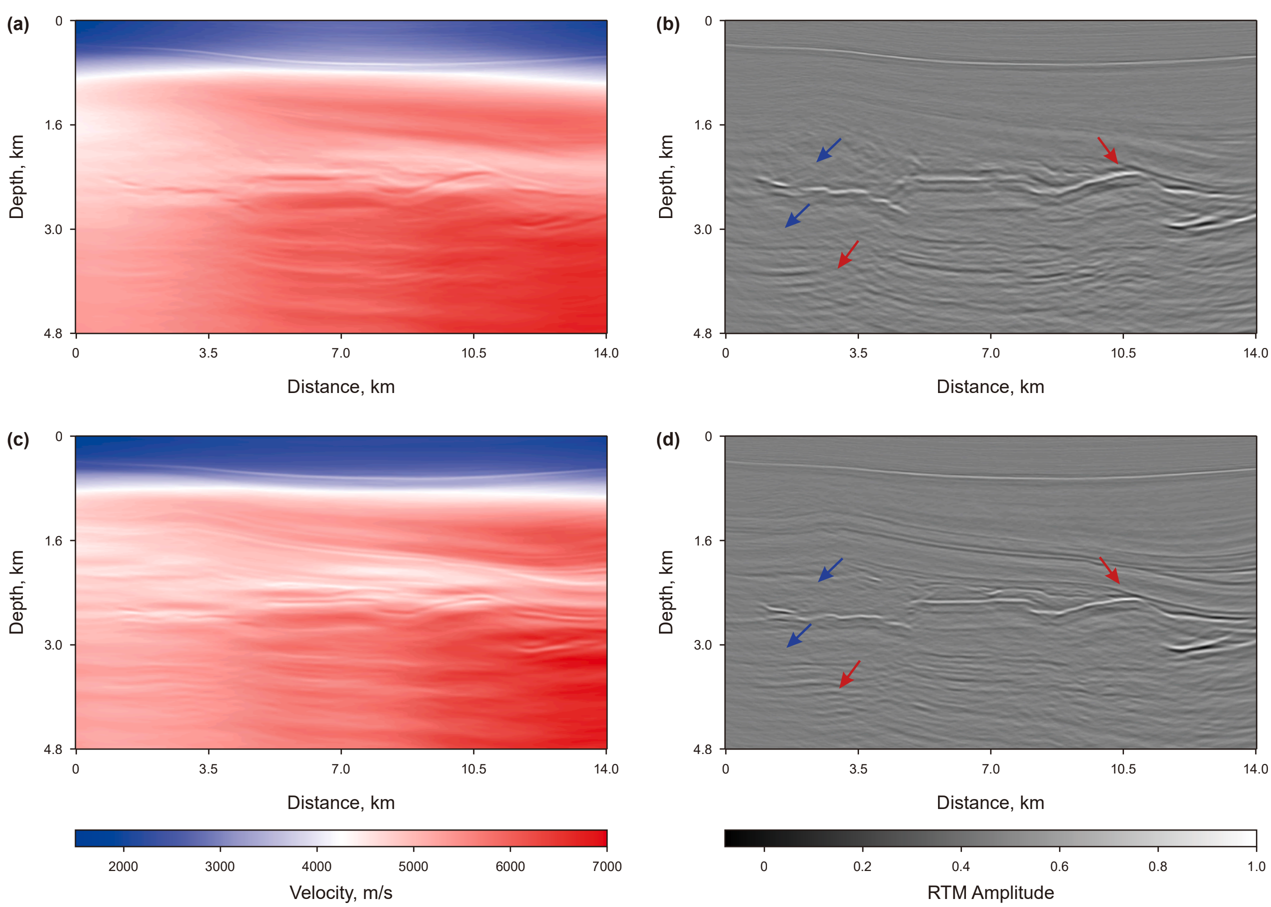

Fig. 13. Comparison of multiscale inversion results for marine seismic data. **(a)** Multi-scale FWI inversion results (25 Hz). **(b)** FWI-imaging result. **(c)** Multi-scale inversion results of PPS-DLI (25 Hz). **(d)** PPS-DLI imaging result.

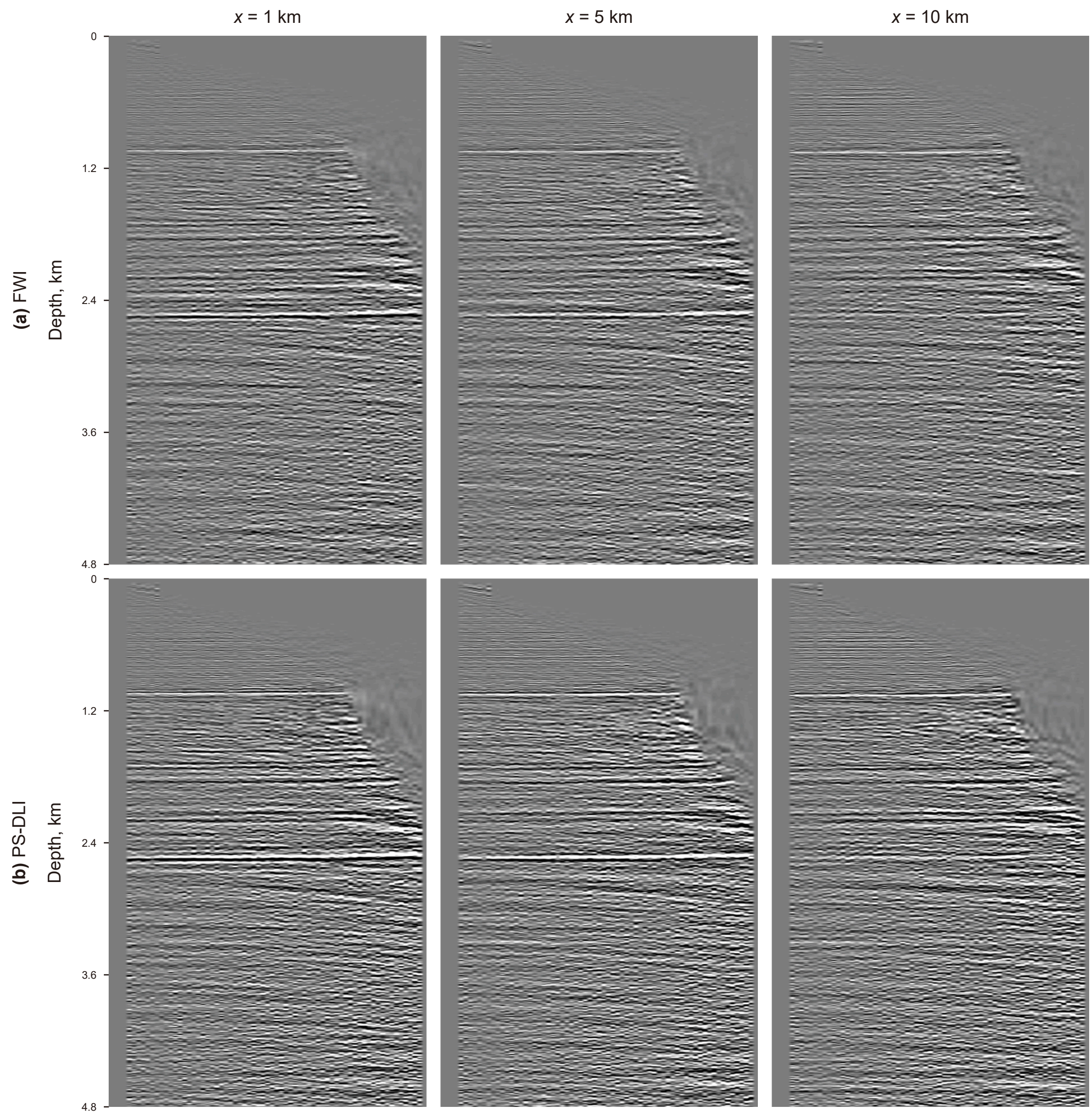

Fig. 14. Common image point (CIP) gathers at three lateral positions ($x = 1$ km, 5 km, 10 km) for the marine field data. **(a)** FWI-imaging results. **(b)** PPS-DLI imaging results. PPS-DLI shows improved event continuity and clarity, particularly in deeper sections.

values. For the velocity reconstruction in deep layers, the method in this paper has obvious advantages, which can reconstruct the background velocity more accurately, and the tectonic features, such as layers and faults, can be better recovered by multiscale inversion to high frequency.

The multiscale PPS-DLI-imaging method (Fig. 13(d)) effectively mitigates migration imaging noise, as indicated by the blue arrow in Fig. 13(b) and (d). In contrast, FWI-imaging retains some residual migration artifacts, a consequence of the adjoint state method used in this paper for gradient computation. This approach relies on the intercorrelation of forward and backward wavefields, inadvertently introducing deep gradient noise into the inversion results during the update process. Furthermore, the PPS-DLI reconstruction in this study provides a clearer depiction of high-frequency geological features (highlighted by the red arrows), owing to the progressive refinement of the background velocity. The deep-layer information is effectively recovered, demonstrating improved continuity over FWI-imaging, thanks to the suppression of migration artifacts and enhanced background velocity.

To further assess the imaging quality improvement, we compare common image point (CIP) gathers at three representative lateral positions (Fig. 14). The PPS-DLI gathers (Fig. 14(b)) exhibit noticeably better event continuity and coherence compared to FWI-imaging (Fig. 14(a)), particularly in the deeper sections below 2.4 km depth. The enhanced clarity of reflection events in PPS-DLI gathers demonstrates that the method not only suppresses migration artifacts in stacked images but also improves the consistency of subsurface reflectors across different imaging angles, which is crucial for reliable seismic interpretation.

4. Conclusion

In this study, we introduce a novel approach to seismic imaging by integrating deep learning with full-waveform inversion (FWI) and migration imaging. Our proposed PPS-DLI framework leverages a progressive self-supervised learning strategy combined with a multi-scale inversion scheme. This method refines velocity models iteratively, starting with low-frequency data to construct robust background velocity models and gradually progressing to higher frequencies for detailed and accurate imaging. The progressive pseudo-label self-supervised strategy enables the dynamic refinement of velocity models by iterating on model segmentation informed by prior network predictions. This results in increasingly accurate velocity models, which are crucial for high-resolution seismic imaging. The multi-scale inversion approach combined with a progressive self-supervised strategy further enhances the method's performance by providing clear illumination of deeper geological features and enabling subsalt imaging, which is often challenging with traditional methods.

Our numerical tests demonstrate the effectiveness of PPS-DLI in addressing key challenges in subsurface imaging. Notably, PPS-DLI significantly reduces migration artifacts compared to traditional migration imaging techniques, leading to cleaner and more accurate seismic images. Additionally, the method preserves amplitude characteristics, facilitating better lithological interpretation through the energy features of imaged axes. This advantage positions PPS-DLI as a superior alternative to conventional migration methods, offering more reliable and interpretable seismic results.

The proposed PPS-DLI method also stands out by offering improved deep structural imaging and sub-salt resolution, making it highly effective for capturing deeper layers of geological features. By mitigating migration artifacts and enhancing deep illumination, our approach enables more precise extraction of subsurface reflection models. These unique capabilities make PPS-DLI a powerful and promising tool for advancing seismic interpretation.

CRediT authorship contribution statement

Wen-Da Li: Writing – review & editing, Writing – original draft, Visualization, Validation, Supervision, Software, Resources, Methodology, Investigation, Formal analysis, Data curation, Conceptualization. **Hao Zhang:** Writing – review & editing, Supervision, Formal analysis. **Shou-Dong Huo:** Writing – review & editing, Investigation, Funding acquisition. **Jian-Guang Han:** Writing – review & editing, Visualization, Resources, Formal analysis.

Conflict of interest

We confirm no conflicts of interest, the work is unpublished and not under other consideration, and all data/code will be made available for reproducibility. We believe this innovation merits publication in your journal and stand ready to provide further details.

Acknowledgments

This work was supported in part by the National Natural Science Foundation of China (Grant Nos. U24B2031, 42174160, 42404134).

Appendix A. Model segmentation method

A spatially-constrained, divisive hierarchical *k*-means parcellation method can parcellate a velocity model into several connected leaf nodes, which can be used as a model basis.

Before the parcellation algorithm starts, we should set a suitable threshold (maximize the number of features), which is about one percent of the velocity model grid points (in this paper is $256 \times 256 \times 0.01 \approx 655$).

In the first step, we use the k-means algorithm to partition the velocity model into two clusters V_1 and V_2 based on their distribution.

$$V = V_1 \cup V_2, \quad V_1 \cap V_2 = \varnothing \tag{5}$$

By minimizing the loss function, we can obtain the above two disjoint clusters V_1 and V_2.

$$Loss(V) = \sum_{i=1}^{2} \sum_{g \in V_i} \left\| v(g) - mean_i \right\|^2 \tag{6}$$

where $v(g)$ is the velocity value at the grid point g, $mean_i$ denotes the velocity mean of V_i.

Secondly, we find the largest spatially connected regions R_1 and R_2 in the clusters V_1 and V_2, where

$$R_1 \subseteqq V_1, \quad \text{and} \quad R_2 \subseteqq V_2 \tag{7}$$

Thirdly, let the regions R_1 and R_2 merge other grid points which belongs to $R_0 = V - V_1 \cup V_2$, respectively.

$$g \in \begin{cases} R_1, & \text{if } Distance_m(g, R_1) \leq Distance_m(g, R_2) \\ R_2, & \text{if } Distance_m(g, R_1) > Distance_m(g, R_2) \end{cases} \tag{8}$$

where $Distance_m$ is Manhattan distance, can be expressed as

$$Distance_m(g, R_i) = \min_{R \in R_i} \left| x_g - x_r \right| + \left| y_g - y_r \right| \tag{9}$$

where x and y are the horizontal and vertical coordinates.

Based on this region's growing algorithm, we divide the model into sub-models A and B, where $V = A \cup B$, $A \cap B = \varnothing$.

In the fourth step, we use the above three steps to repeatedly parcel the sub-models until the number of grid points of the sub-model $g \leq Threshold$. When the cycle-parcellation ends, we get the corresponding leaf nodes with $g \leq Threshold$, which we use as the model basis. Then we will get a series of leaf nodes, which can be jointly reconstructed $V = \{R_1, R_2, \ldots, R_n\}$; $R_1 \cap R_2 \cap \cdots \cap R_n = \varnothing$.

The last step is to construct several different training velocities from the above model basis. The random training velocity model $\widehat{V}_n$ are set by assigning random values ($\widehat{val} \sim Nor[E(R_i), Var(r_i)]$) for every model basis (leaf nodes), based on the mean $E(R_i) = \frac{1}{N_i}\sum_{r \in R_i} r$ and variance $Var(r_i) = \frac{1}{N_i}\sum_{r \in R_i}[r - E(r_i)]^2$, where i = 1, 2, ..., n and *Nor* denotes a normal distribution.

Appendix B. Network structure

In this paper, we use an attention U-Net to introduce some attention layers into a standard U-Net. We can improve the network's attention to structures such as faults and layers based on the attention layers, thus improving the accuracy of the inversion of subsurface structures. Fig. 15 shows the structure the attention U-Net in this paper. The specific structure of the network was described in our previous paper Li et al. (2022).

The attention U-Net is a potent neural network comprising diverse elements, encompassing downsampling and upsampling strata, skip connections, and attention strata. The encoder segment of the network is fashioned using Conv, ReLU, and downsampling strata. The encoder and decoder segments of the network share an asymmetrical structure. Additionally, the attention strata augment the precision of the network by concentrating on the most informative attributes throughout the training procedure.

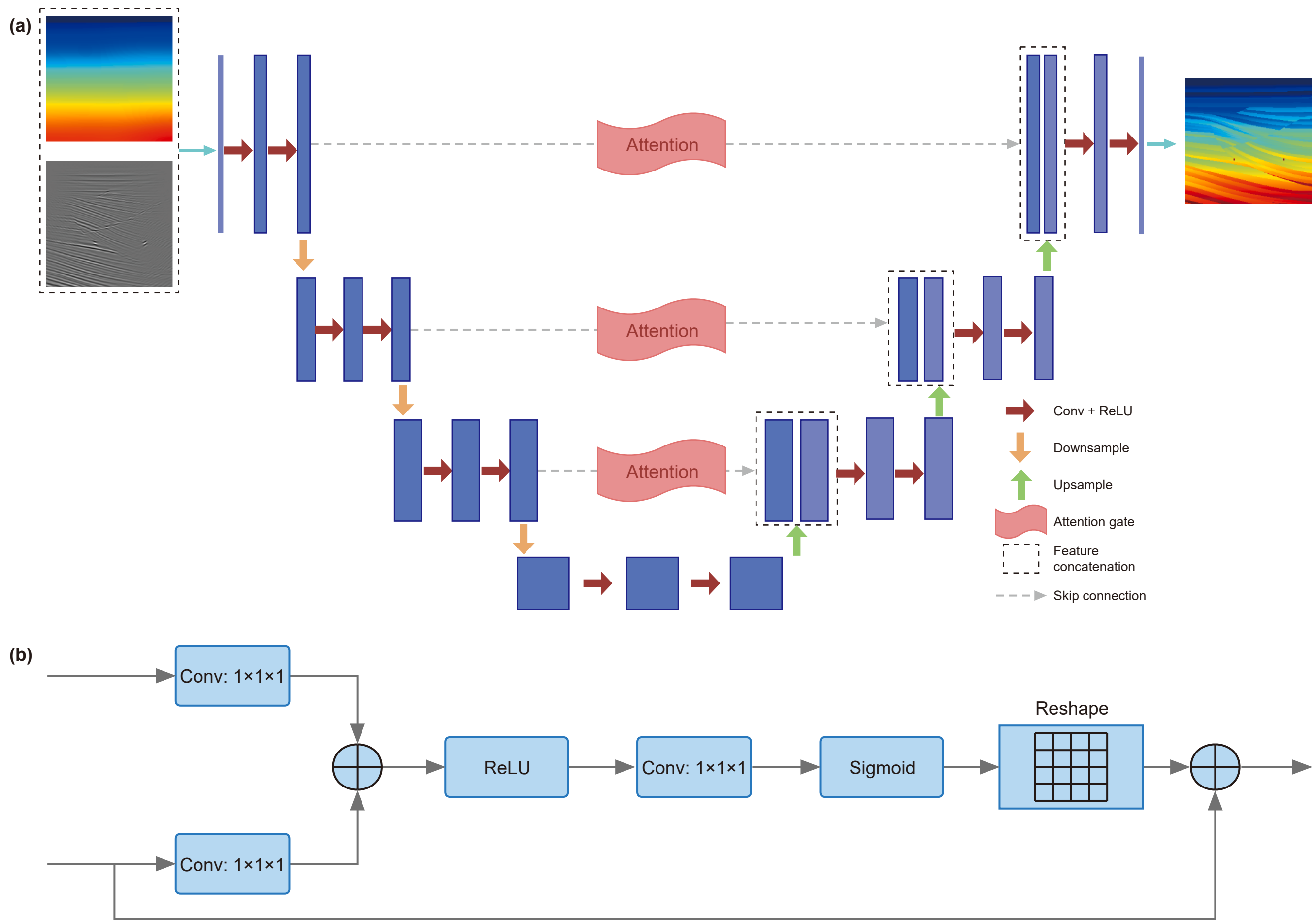

Fig. 15. The structure of the attention U-Net in this paper. (**a**) A standard U-Net with some attention gates. (**b**) The inner structure of an attention gate.

The attention U-Net is a powerful neural network that consists of various components, including downsampling and upsampling layers, skip connections, and attention layers. The encoder part of the network is constructed using Conv, ReLU, and downsampling layers, where Maxpooling is used as the downsampling layer. The encoder and decoder parts of the network have an asymmetric structure in common. Furthermore, the attention layers enhance the accuracy of the network by focusing on the most informative features during the training process. Overall, the attention U-Net is a powerful tool that can be used in various applications, including image segmentation and classification, due to its ability to extract and utilize important features from the input data. In this paper, we choose an attention U-Net as the basic structure of PPS-DLI, which can greatly improve the inversion accuracy.

References

Alkhalifah, T., Choi, Y., 2014. From tomography to full-waveform inversion with a single objective function. Geophysics 79 (2), R55–R61. https://doi.org/10.1190/geo2013-0291.1.

Berti, S., Aleardi, M., Stucchi, E., 2024. A computationally efficient bayesian approach to full-waveform inversion. Geophys. Prospect. 72, 580–603. https://doi.org/10.1111/1365-2478.13437.

Bunks, C., Saleck, F.M., Zaleski, S., Chavent, G., 1995. Multiscale seismic waveform inversion. Geophysics 60, 1457–1473. https://doi.org/10.1190/1.1443880.

Cheng, S., Wang, Y., Zhang, Q., Harsuko, R., Alkhalifah, T., 2024. A self-supervised learning framework for seismic low-frequency extrapolation. Journal of Geophysical Research: Machine Learning and Computation 1 (3) e2024JH000157. https://doi.org/10.1029/2024JH000157.

Chi, B., Dong, L., Liu, Y., 2014. Full waveform inversion method using envelope objective function without low frequency data. Journal of Applied Geophysics 109, 36–46. https://doi.org/10.1016/j.jappgeo.2014.07.010.

Choi, Y., Alkhalifah, T., 2011. Source-independent time-domain waveform inversion using convolved wavefields: Application to the encoded multisource waveform inversion. Geophysics 76 (5), R125–R134. https://doi.org/10.1190/geo2010-0210.1.

Claerbout, J.F., 1971. Toward a unified theory of reflector mapping. Geophysics 36 (3), 467–481. https://doi.org/10.1190/1.1440185.

Fang, J., Chen, H., Zhou, H., Rao, Y., Sun, P., Zhang, J., 2020. Elastic full-waveform inversion based on GPU accelerated temporal fourth-order finite-difference approximation. Computers & Geosciences 135, 104381. https://doi.org/10.1016/j.cageo.2019.104381.

Fang, J., Zhou, H., Elita Li, Y., Shi, Y., Li, X., Wang, E., 2024. Deep-learning optimization using the gradient of a custom objective function: A full-waveform inversion example study on the convolutional objective function. Geophysics 89, R479–R492. https://doi.org/10.1190/geo2023-0538.1.

Fu, L., Guo, B., Schuster, G.T., 2018. Multiscale phase inversion of seismic data. Geophysics 83, R159–R171. https://doi.org/10.1190/geo2017-0353.1.

Guo, Y., Huang, J., Cui, C., Li, Z., Fu, L., Li, Q., 2019. Multi-source multi-scale source-independent full waveform inversion. J. Geophys. Eng. 16, 479–492. https://doi.org/10.1093/jge/gxz013.

Ha, W., Shin, C., 2021. Deconvolution-based objective functions for full waveform inversion in the laplace domain. IEEE Trans. Geosci. Rem. Sens. 60, 1–8. https://doi.org/10.1109/TGRS.2021.3085512.

He, Q., Wang, Y., 2021. Reparameterized full-waveform inversion using deep neural networks. Geophysics 86, V1–V13. https://doi.org/10.1190/geo2019-0382.1.

Huang, R., Zhang, Z., Wu, Z., Wei, Z., Mei, J., Wang, P., 2021. Full-waveform inversion for full-wavefield imaging: decades in the making. Lead. Edge 40, 324–334. https://doi.org/10.1190/tle40050324.1.

Jiang, P., Wang, Q., Ren, Y., Yang, S., Li, N., 2023. Full waveform inversion based on inversion network reparameterized velocity. Geophys. Prospect. 72, 52–67. https://doi.org/10.1111/1365-2478.13292.

Lailly, P., 1983. The Seismic Inverse Problem as a Sequence of before Stack Migrations. In: Bednar, J.B., Robinson, E., Weglein, A. (Eds.), Conference on Inverse Scattering: Theory and Application. SIAM, Philadelphia, pp. 206–220.
Liu, D.J., Huang, J.P., Wang, Z.Y., 2020. Convolution-based multi-scale envelope inversion. Pet. Sci. 17, 352–362. https://doi.org/10.1007/s12182-019-00419-8.
Li, W., Wu, T., Liu, H., 2022. Structure-preserving random noise attenuation method for seismic data based on a flexible attention cnn. Remote Sens 14, 5240. https://doi.org/10.3390/rs14205240.
Liu, B., Yang, S., Ren, Y., Xu, X., Jiang, P., Chen, Y., 2021. Deep-learning seismic full-waveform inversion for realistic structural models. Geophysics 86, R31–R44. https://doi.org/10.1190/geo2019-0435.1.
Lu, R., 2016. Revealing overburden and reservoir complexity with high-resolution FWI. In: SEG International Exposition and Annual Meeting. https://doi.org/10.1190/segam2016-13872562.1.
McLeman, J., Rayment, T., Burgess, T., Dancer, K., Hampson, G., Pauli, A., 2023. Superior resolution through multiparameter fwi imaging: a new philosophy in seismic processing and imaging. Lead. Edge 42, 34–43. https://doi.org/10.1190/tle42010034.1.
Nie, Z., Feng, B., Wang, H., Xu, R., 2025. Multi-scale full waveform inversion based on gradient bidimensional empirical mode decomposition. Geophysics 90, 1–88. https://doi.org/10.1190/geo2024-0267.1.
Plotnitskii, P., Kazei, V., Ovcharenko, O., Peter, D., Alkhalifah, T., 2020. Extrapolation of low wavenumbers in FWI gradients by a deep convolutional neural network. In: EAGE 2020 Annual Conference & Exhibition Online. European Association of Geoscientists & Engineers, pp. 1–5.
Qu, Y., Li, Z., Huang, J., Li, J., 2018. Multi-scale full waveform inversion for areas with irregular surface topography in an auxiliary coordinate system. Explor. Geophys. 49, 68–80. https://doi.org/10.1071/EG16037.
Rasht-Behesht, M., Huber, C., Shukla, K., Karniadakis, G.E., 2022. Physics-informed neural networks (PINNs) for wave propagation and full waveform inversions. J. Geophys. Res. Solid Earth 127 e2021JB023120. https://doi.org/10.1029/2021JB023120.
Schuster, G.T., Chen, Y., Feng, S., 2024. Review of physics-informed machine-learning inversion of geophysical data. Geophysics 89, T337–T356. https://doi.org/10.1190/geo2023-0615.1.
Shen, X., Jiang, L., Dellinger, J., Brenders, A., Kumar, C., James, M., Etgen, J., Meaux, D., Walters, R., Abdullayev, N., 2018. High resolution full waveform inversion for structural imaging in exploration. In: SEG International Exposition and Annual Meeting. https://doi.org/10.1190/segam2018-2997202.1.
Sirgue, L., Barkved, O., Van Gestel, J., Askim, O., Kommedal, J., 2009. 3D waveform inversion on valhall wide-azimuth OBC. In: 71st EAGE Conference and Exhibition Incorporating.. https://10.3997/2214-4609.201400395.
Song, C., Alkhalifah, T., 2021. Wavefield reconstruction inversion via physics-informed neural networks. IEEE Trans. Geosci. Rem. Sens. https://doi.org/10.1109/TGRS.2021.3123122.
Tarantola, A., 1984. Inversion of seismic reflection data in the acoustic approximation. Geophysics 49, 1259–1266. https://doi.org/10.1190/1.1441754.
Taufik, M.H., Wang, F., Alkhalifah, T., 2024. Learned regularizations for multi-parameter elastic full waveform inversion using diffusion models. J. Geophys. Res.: Machine Learning and Computation 1 e2024JH000125. https://doi.org/10.1029/2024JH000125.
Virieux, J., Operto, S., 2009. An overview of full-waveform inversion in exploration geophysics. Geophysics 74, WCC1–WCC26. https://doi.org/10.1190/1.3238367.
Waheed, U.b., Alkhalifah, T., Haghighat, E., Song, C., Virieux, J., 2021. PINNtomo: Seismic tomography using physics-informed neural networks. arXiv preprint arXiv:2104.01588. https://doi.org/10.48550/arXiv.2104.01588.
Wang, B., Gao, J., Zhang, H., Zhao, W., 2011. Cuda-based acceleration of full waveform inversion on GPU. In: SEG Technical Program Expanded Abstracts 2011. Society of Exploration Geophysicists, pp. 2528–2533.
Wang, L., Min, F., Pan, S., Song, G., Tan, L., Wang, K., 2024a. FWI-WF: Robust full-waveform inversion using hybrid Wasserstein-1 and Fourier metrics. Geophysics 89 (6), F117–F128. https://doi.org/10.1190/geo2024-0056.1.
Wang, Y., Jiang, B., Wei, Z., Lu, W., 2023. Deep velocity generator: A plug-in network for FWI enhancement. IEEE Trans. Geosci. Rem. Sens. 61, 1–17. https://doi.org/10.1109/TGRS.2023.3247880.
Wang, W., Ma, J., 2020. Velocity model building in a crosswell acquisition geometry with image-trained artificial neural networks. Geophysics 85, U31–U46. https://doi.org/10.1190/geo2018-0591.1.
Wang, W., Wu, Y., Wang, Y., McMechan, G.A., 2024b. Leveraging self-supervised deep learning to address cross-talks in multi-parameter inversions. In: Fourth International Meeting for Applied Geoscience & Energy, pp. 827–831. https://doi.org/10.1190/image2024-4093253.1.
Wang, P., Zhang, Z., Mei, J., Lin, F., Huang, R., 2019. Full-waveform inversion for salt: A coming of age. Lead. Edge 38, 204–213. https://doi.org/10.1190/tle38030204.1.
Wu, Y., Lin, Y., Zhou, Z., 2018. Inversionnet: Accurate and efficient seismic waveform inversion with convolutional neural networks. In: SEG Technical Program Expanded Abstracts 2018, pp. 2096–2100. https://doi.org/10.1190/segam2018-2998603.1.
Wu, Y., McMechan, G.A., 2019. Parametric convolutional neural network-domain full-waveform inversion. Geophysics 84, R881–R896. https://doi.org/10.1190/geo2018-0224.1.
Wu, Y., McMechan, G.A., Wang, Y., 2021. CNN-based gradient-free multiparameter reflection full-waveform inversion. In: First International Meeting for Applied Geoscience & Energy. https://10.1190/segam2021-3593600.1.
Wu, Y., McMechan, G.A., Wang, Y., 2022. Adaptive feedback convolutional-neural-network-based high-resolution reflection-waveform inversion. J. Geophys. Res. Solid Earth 127. https://doi.org/10.1029/2022JB024138.
Yang, F., Ma, J., 2019. Deep-learning inversion: A next-generation seismic velocity model building method. Geophysics 84, R583–R599. https://doi.org/10.1190/geo2018-0249.1.
Zhang, W., Gao, J., 2021. Deep-learning full-waveform inversion using seismic migration images. IEEE Trans. Geosci. Rem. Sens. 60, 1–18. https://doi.org/10.1109/TGRS.2021.3062688.
Zhang, W., Gao, J., Gao, Z., Chen, H., 2021. Adjoint-driven deep-learning seismic full-waveform inversion. IEEE Trans. Geosci. Rem. Sens. 59 (10), 8913–8932.
Zhang, Z., Wu, Z., Wei, Z., Mei, J., Huang, R., Wang, P., 2020. FWI imaging: Full-wavefield imaging through full-waveform inversion. In: SEG International Exposition and Annual Meeting. D031S027R004. https://doi.org/10.1190/segam2020-3427858.1.
Zhang, Y., Zhu, X., Gao, J., 2023. Seismic inversion based on acoustic wave equations using physics-informed neural network. In. IEEE Trans. Geosci. Rem. Sens. 61, 1–11. https://doi.org/10.1109/TGRS.2023.3236973.
Zhao, P., Fang, J., Jie, C., Zhang, J., Wang, E., Zhang, S., 2025. Multiscale deep learning reparameterized full waveform inversion with the adjoint method. IEEE Trans. Geosci. Rem. Sens. https://doi.org/10.1109/TGRS.2025.3553053.
Zhu, W., Xu, K., Darve, E., Biondi, B., Beroza, G.C., 2022. Integrating deep neural networks with full-waveform inversion: Reparameterization, regularization, and uncertainty quantification. Geophysics 87, R93–R109. https://doi.org/10.1190/geo2020-0933.1.